

In addition, there is a very bright, physically disconnected, feature inside the downside oval, at the footprint of polar-cap field lines. It extends polewards up to $\sim 78^\circ$ S ($\sim 6^\circ$ poleward of the oval), and is confined to the 5:30–11:00 local time sector. Its peak brightness (95 kR) largely exceeds that of the oval and its total auroral output, 2.4×10^{10} watts, is comparable to the oval output despite its very limited spatial extent.

This suggests that, in response to the passage of the shock, the auroral oval mainly brightens at both planets on the night side, at the footprint of magnetotail magnetic field lines. However, Saturn does not exhibit the expansion towards lower latitudes that is typical of the geomagnetic storm oval. As for the bright polar-cap feature, it does not seem to have any terrestrial counterpart. It is reminiscent of the terrestrial polar cusp, frequently observed during dayside reconnection of closed field lines with the IMF, on or slightly poleward of the oval, and which is detected as a variable feature on Jupiter as well²⁶. But, in contrast to the saturnian feature, the terrestrial polar cusp is close to noon²⁷.

Recent studies, however, indicate that the IMF By east–west component (that is, dawn–dusk on Saturn) has a strong influence on the local-time position of the cusp and may shift it towards morning or afternoon by as much as several hours^{28,29}. Even though polar cusps on Earth have not been observed as far as 6:00 local time, this is an issue that should be investigated. Unfortunately, the direction of the IMF cannot be extrapolated as the other solar-wind properties can be. Another interpretation could be that strong reconnection at Saturn does not occur on the day side, but rather on the morning flank of the magnetopause, where it has been suggested that a Kelvin–Helmholtz instability triggers the saturnian auroral radio emissions³⁰. It will be possible to check these hypotheses with local plasma measurements taken at Saturn by the Cassini mission. □

Received 14 May; accepted 27 August 2004; doi:10.1038/nature02986.

1. de Mairan, J. J. *Traité Physique et Historique de l'Aurore Boréale* 245–279 (Mémoire de l'Académie Royale des Sciences, Imprimerie Royale, Paris, 1733).
2. Chapman, S. & Ferraro, V. C. A. A new theory of magnetic storms. *Nature* **126**, 129 (1930); *Terr. Magn. Atmos. Electr.* **36**, 171–186 (1931); *Terr. Magn. Atmos. Electr.* **37**, 147–156 (1932).
3. Licht, A. L. Properties of the solar wind during sunspot minimum. *J. Geophys. Res.* **65**, 1397–1400 (1960).
4. Greenstadt, E. W. Interplanetary magnetic effects of solar flares: Explorer 18 and Pioneer 5. *J. Geophys. Res.* **70**, 5451–5452 (1965).
5. Snyder, C. W., Neugebauer, M. & Rao, U. R. The solar wind velocity and its correlation with cosmic-ray variations and with solar and geomagnetic activity. *J. Geophys. Res.* **68**, 6361–6370 (1963).
6. Axford, W. I. The interaction between the solar wind and the earth's magnetosphere. *J. Geophys. Res.* **67**, 3791–3796 (1962).
7. Carr, T. D. Jupiter's decametric rotation period and the source A emission beam. *Phys. Earth Planet. Inter.* **6**, 21–28 (1972).
8. Zarka, P. Auroral radio emissions at the outer planets: Observations and theories. *J. Geophys. Res.* **103**, 20159–20194 (1998).
9. Broadfoot, A. L. *et al.* Extreme ultraviolet observations from Voyager 1 encounter with Jupiter. *Science* **204**, 979–982 (1979).
10. Clarke, J. T. *et al.* Spatial imaging of hydrogen Lyman-alpha emission from Jupiter. *Astrophys. J.* **240**, 696–701 (1980).
11. Broadfoot, A. L. *et al.* Extreme ultraviolet observations from Voyager 1 encounter with Saturn. *Science* **212**, 206–211 (1981).
12. Gallagher, D. L. & D'Angelo, N. Correlation between solar wind parameters and auroral kilometric radiation intensity. *Geophys. Res. Lett.* **8**, 1087–1089 (1981).
13. Zarka, P. & Genova, F. Low-frequency jovian emission and solar wind magnetic sector structure. *Nature* **306**, 767–768 (1983).
14. Desch, M. D. & Barrow, C. H. Direct evidence for solar wind control of Jupiter's hectometer wavelength radio emission. *J. Geophys. Res.* **89**, 6819–6823 (1984).
15. Rabl, G. K. F. Periodicities of jovian broad-band kilometric radiation observed by Ulysses. *Planet. Space Sci.* **41**, 1079–1083 (1993).
16. Desch, M. D. & Rucker, H. O. The relationship between Saturn kilometric radiation and the solar wind. *J. Geophys. Res.* **88**, 8999–9006 (1983).
17. Cowley, S. H. W., Bunce, E. J. & Prangé, R. Saturn's polar ionospheric flows and their relation to the main auroral oval. *Ann. Geophys.* **22**, 2685–2688 (2004).
18. Vasylunas, V. M. in *Physics of the Jovian Magnetosphere* (ed. Dessler, A. J.) 395–453 (Cambridge Univ. Press, Cambridge, UK, 1990).
19. Prangé, R. *et al.* Detailed study of FUV Jovian auroral features with the post COSTAR Hubble Faint Object Camera. *J. Geophys. Res.* **103**, 20195–20210 (1998).
20. Pallier, L. & Prangé, R. More about the structure of the high latitude Jovian aurorae. *Planet. Space Sci.* **49**, 1159–1173 (2001).
21. Gurnett, D. A. *et al.* Control of Jupiter's radio emission and aurorae by the solar wind. *Nature* **415**, 985–987 (2002).

22. Trauger, J. *et al.* Saturn's hydrogen aurora: Wide field and planetary camera 2 imaging from the Hubble Space Telescope. *J. Geophys. Res.* **103**, 20237–20244 (1998).
23. Tóth, G. *Versatile Advection Code*; code available at (<http://www.phys.uu.nl/~toth>) (1994).
24. Hanlon, P. G. *et al.* On the evolution of the solar wind between 1 and 5 AU at the time of the Cassini Jupiter flyby: Multispacecraft observations of interplanetary coronal mass ejections including the formation of a merged interaction region. *J. Geophys. Res.* **109**, doi:10.1029/2003A010112 (2004).
25. Frank, L. A. & Craven, J. D. Imaging results from Dynamics Explorer. *Rev. Geophys.* **26**, 249–283 (1988).
26. Pallier, L. & Prangé, R. Detection of the southern counterpart of the jovian northern polar cusp. Shared properties. *Geophys. Res. Lett.* **31**, doi:10.1029/2003GL018041 (2004).
27. Lockwood, M. *et al.* The ionospheric signature of flux transfer events and solar wind dynamic pressure changes. *J. Geophys. Res.* **95**, 17113–17135 (1990).
28. Sandholz, P. E., Farrugia, C. J., Moen, J., Cowley, S. W. H. & Lybekk, B. Dynamics of the aurora and associated currents during a cusp bifurcated event. *Geophys. Res. Lett.* **25**, 4313–4316 (1981).
29. Milan, S. E., Lester, M., Cowley, S. W. H. & Brittacher, M. Dayside convection and auroral morphology during an interval of northward interplanetary magnetic field. *Ann. Geophys.* **18**, 436–444 (2004).
30. Galopeau, P. H. M., Zarka, P. & Le Quéau, D. Source location of Saturn's kilometric radiation: The Kelvin–Helmholtz instability hypothesis. *J. Geophys. Res.* **100**, 26337–26410 (1998).

Acknowledgements This work is based partly on observations with the NASA/ESA HST obtained at the STScI, which is operated by the AURA, Inc. for NASA.

Competing interests statement The authors declare that they have no competing financial interests.

Correspondence and requests for materials should be addressed to R.P. (renee.prange@obspm.fr).

Optically programmable electron spin memory using semiconductor quantum dots

Miro Kroutvar, Yann Ducommun, Dominik Heiss, Max Bichler, Dieter Schuh, Gerhard Abstreiter & Jonathan J. Finley

Walter Schottky Institut, Technische Universität München, Am Coulombwall 3, D-85748 Garching, Germany

The spin of a single electron subject to a static magnetic field provides a natural two-level system that is suitable for use as a quantum bit, the fundamental logical unit in a quantum computer^{1–3}. Semiconductor quantum dots fabricated by strain driven self-assembly⁴ are particularly attractive for the realization of spin quantum bits, as they can be controllably positioned⁵, electronically coupled⁶ and embedded into active devices^{7–10}. It has been predicted that the atomic-like electronic structure⁴ of such quantum dots suppresses coupling of the spin to the solid-state quantum dot environment^{11–14}, thus protecting the ‘spin’ quantum information against decoherence^{15,16}. Here we demonstrate a single electron spin memory device in which the electron spin can be programmed by frequency selective optical excitation. We use the device to prepare single electron spins in semiconductor quantum dots with a well defined orientation, and directly measure the intrinsic spin flip time and its dependence on magnetic field. A very long spin lifetime is obtained, with a lower limit of about 20 milliseconds at a magnetic field of 4 tesla and at 1 kelvin.

We begin by summarizing the operating principles of our optical spin storage device before presenting the measurements of the spin flip time, its dependence on magnetic field and the determination of the underlying mechanism. The structure of the devices investigated and the measurement techniques are summarized in Fig. 1. The samples consist of a single layer of self-assembled Ga(In)As quantum dots (QDs) embedded within the intrinsic region of a p-type GaAs Schottky photodiode¹⁷. Single electron–hole pair excitations (excitons) are generated directly in QD ground states by frequency-

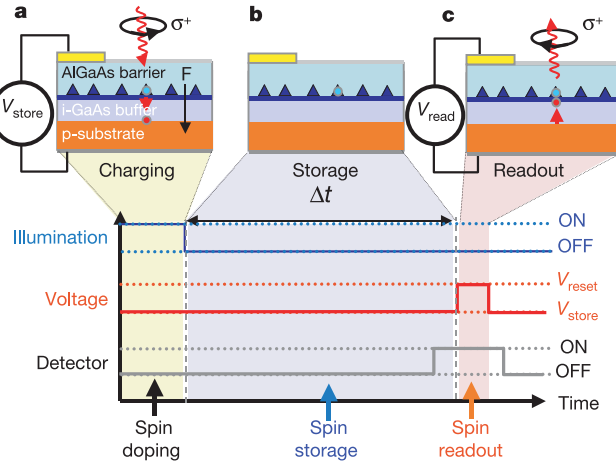


Figure 1 Schematic of devices and operation principle. **a**, Following resonant excitation into QD ground states, excitons are ionized owing to the axial electric field provided by the applied bias (V_{store}). The AlGaAs barrier above the QD layer inhibits electron escape from the QDs, ensuring photon-to-charge conversion. **b**, After charge separation, electrons are stored directly in the QDs where they were generated. **c**, Readout of the stored charge distribution by forward biasing the device ($V = V_{\text{read}}$). Holes drift back into the QDs, neutralizing the stored charge and generating a photon, the polarization of which probes the electron spin orientation—see Supplementary Information for further details.

selective optical excitation on the low-energy side of the QD ensemble. Photon-to-charge conversion is ensured by the electric field in the intrinsic region of the device ($\sim 160 \text{ kV cm}^{-1}$) orientated parallel to the QD growth axis. This results in holes tunnelling out of the QDs over timescales much faster than the exciton radiative lifetime⁸, while electrons remain stored owing to the presence of an asymmetric Ga_{0.6}Al_{0.4}As barrier grown immediately above the QDs (Fig. 1a). Our previous measurements¹⁷ have confirmed that this technique enables selective generation of single electrons directly in the QD ground state where they remain over timescales of up to hours at low temperature (Fig. 1b)¹⁸. Generation of only one electron per dot is ensured by the few milli-electronvolt renormalization of the inter-band absorption energy following charging¹⁹.

Following a delay time Δt , the stored electron distribution is optically probed by forward biasing the Schottky junction, as depicted schematically in Fig. 1c. A drift current of holes then flows into the negatively charged dots and neutralizes the stored charge. The electron–hole pairs in the QDs then rapidly recombine over the radiative recombination time ($\approx 1 \text{ ns}$), generating a time-delayed electroluminescence (EL) signal that directly reflects the spectral distribution of stored charge a time Δt after generation. A single photon counter is gated ON immediately before the reset voltage pulse to detect the emitted photons and OFF again after $\tau_{\text{det}} \approx 500 \text{ ns}$ (Fig. 1), after which the exciton population has decayed completely. Further details of the device operation and experimental techniques can be found in Supplementary Information.

To extend the concepts introduced above from photon-to-charge conversion to optically induced electron spin orientation, a key consideration is the spin structure of the QD ground state exciton. The QD exciton states are constructed from electron (e) and heavy-hole (h) single-particle basis states with spin projections along the QD growth axis (z) of $J_{e,z} = +1/2\hbar$ or $-1/2\hbar$ ($e \uparrow$ or $e \downarrow$) and $J_{h,z} = -3/2\hbar, +3/2\hbar$ ($h \downarrow$ and $h \uparrow$) respectively²⁰. As a circularly polarized photon conveys one unit of angular momentum (+1 \hbar for σ^+ and -1 \hbar for σ^-) and the optical transition takes place to the crystal ground state, only the exciton states with $J_z = J_{e,z} + J_{h,z} = \pm 1\hbar$ ($e \downarrow h \uparrow$ and $e \uparrow h \downarrow$) are optically active. However, the $e \uparrow h \downarrow$

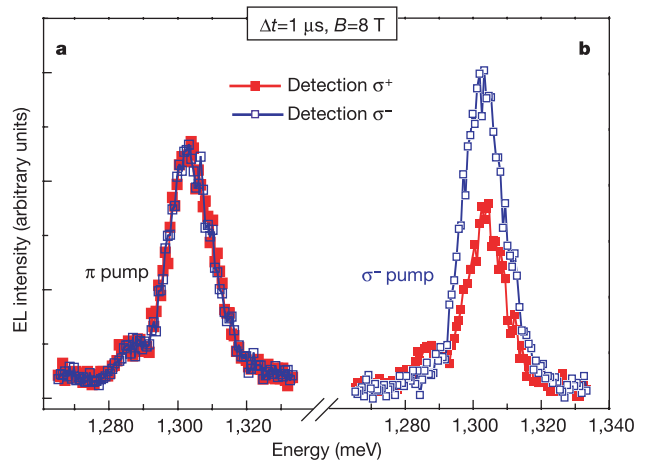


Figure 2 Spin storage spectra for $T = 10 \text{ K}$, high magnetic field $B = 8 \text{ T}$ and a short storage time of $\Delta t = 1 \mu\text{s}$. **a**, After randomly linearly polarized excitation, EL intensities for σ^+ (red, filled squares) and σ^- (blue, open squares) are equal. Both spin orientations are created equally. No thermalization into the lower Zeeman level occurs. **b**, Following σ^- excitation, co-polarized σ^- EL intensity (blue, open squares) is enhanced versus the counter-polarized σ^+ light (red, filled squares). Selective pumping of one Zeeman level exhibits a long-term spin memory: an approximately 65% degree of co-polarization for the data presented, eventually becoming as large as $\sim 85\%$ at $T = 1 \text{ K}$.

and $e \downarrow h \uparrow$ eigenstates are often mixed in dots with reduced symmetry, forming two linearly polarized eigenstates separated by the anisotropic e–h exchange splitting of a few times $10 \mu\text{eV}$ (δ_1) (refs 20, 21). In order to enable optical selection of pure spin states, all the measurements described below were performed with large static magnetic fields ($B \geq 4 \text{ T}$) applied parallel to the growth axis of the dots. This results in a Zeeman splitting $\Delta E_Z^{\text{ex}} = g^* \mu_B B$ of the QD exciton levels, where g^* is the excitonic g-factor. This transforms them into pure $e \uparrow h \downarrow$ and $e \downarrow h \uparrow$ eigenstates, providing that $\Delta E_Z^{\text{ex}} > \delta_1$ (ref. 20). Optical excitation using circularly polarized light with σ^- or σ^+ helicity then selectively generates electrons with up ($e \uparrow$) or down ($e \downarrow$) spin orientation, respectively. When the spin is read out after a time delay Δt , the degree of circular polarization of the emitted EL intensity (I), $P = (I^{\sigma^+} - I^{\sigma^-})/(I^{\sigma^+} + I^{\sigma^-})$, then provides a direct probe of the electron spin orientation a time Δt after generation.

In order to verify the concepts introduced above, we performed spin storage measurements for a short delay time ($\Delta t = 1 \mu\text{s}$) and large magnetic field ($B = 8 \text{ T}$), while varying the polarization state of the excitation source. Figure 2 compares typical storage spectra recorded at $T = 10 \text{ K}$ following excitation with randomly linearly (left panel) or σ^- circularly polarized light (right panel). By comparing the frequency and spatially selective nature of the excitation process, we estimate that $\sim 10,000$ dots are addressed by the measurement (see Supplementary Information). Following linear excitation, the storage spectra detected with σ^- and σ^+ polarization are equally intense because both spin orientations ($e \uparrow$ and $e \downarrow$) are generated with equal probability in the QDs. The lack of any circular polarization excludes the possibility that spin alignment due to inter Zeeman level thermalization occurs over such short storage times. In contrast, following σ^- excitation to generate $e \uparrow$ electrons in the lower Zeeman level, the storage EL is found to be strongly co-polarized (Fig. 2, right panel). At 10 K and $B = 8 \text{ T}$, the measured degree of circular polarization following σ^- excitation ($P(\sigma^-)$) was as large as $\sim -65\%$, but was found to increase strongly (up to $\sim -85\%$) with reducing temperature as discussed below. Repeating this measurement using σ^+ excitation to generate a population of $e \downarrow$ electrons in the upper Zeeman level again produced co-polarized emission, but with precisely the

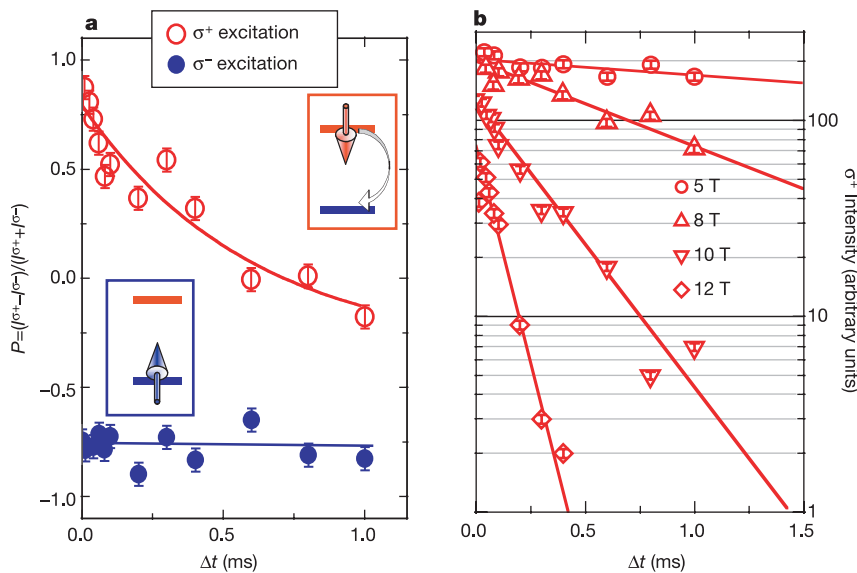


Figure 3 Electron spin dynamics at $T = 1\text{ K}$ and $B = 8\text{ T}$ for storage times up to 1 ms. **a**, The degree of circular polarization (P) at peak of the storage EL. Red: pumping electron spins into the upper Zeeman level. Temporal decay observed from co-polarized emission ($P > 0$) at short delay times to counter-polarized emission ($P < 0$) after $\Delta t > 0.75\text{ ms}$. Blue: pumping electrons into the lower Zeeman level results in co-polarized emission

opposite degree of circular polarization, $P(\sigma^+) \approx +65\%$. These results demonstrate that the storage signal exhibits a pronounced polarization memory for both spin orientations, arising from the reversible transfer from optical polarization to electron spin orientation (Fig. 1a) followed by spin storage for a time Δt (Fig. 1b) and back-transfer from electron spin orientation into optical polarization (Fig. 1c).

Following demonstration of this spin memory effect, we now consider the temporal evolution of $P(\sigma^+)$ and $P(\sigma^-)$, a measurement that reflects the electron spin dynamics in the QDs during the storage time (Δt). Figure 3a shows the degree of circular polarization of the storage EL, monitored at the peak position as a function of storage time in the range $0.001 < \Delta t (\text{ms}) < 1$ at $B = 8\text{ T}$ and a reduced lattice temperature of $T = 1\text{ K}$. $P(\sigma^-)$ was found to be as large as -85% with no detectable temporal evolution up to 1 ms (Fig. 3a, lower curve). In contrast, a very marked time evolution of $P(\sigma^+)$ is observed (Fig. 3a, upper curve). For $\Delta t \approx 0.001\text{ ms}$, $P(\sigma^+)$ is as large as $+85\%$, decaying over time to $\sim -10\%$ at $\Delta t \approx 1\text{ ms}$, as electrons relax from the upper to the lower Zeeman levels. At thermal equilibrium, the population ratio of the upper and lower Zeeman levels is $N_\uparrow/N_\downarrow = \exp(-g_e^*\mu_B B/k_B T)$, indicating that $N_\uparrow/N_\downarrow < 0.02$ under the present experimental conditions ($g_e^*\mu_B B \approx 0.36\text{ meV}$ and $k_B T \approx 0.09\text{ meV}$). Therefore, the contrast of the observed decay from the upper level (N_\uparrow) is much larger, while spin flip mechanisms for $e\downarrow \Rightarrow e\uparrow$ and $e\uparrow \Rightarrow e\downarrow$ remain the same. To confirm this interpretation, we reversed the orientation of the magnetic field to invert the energetic ordering of the Zeeman levels. In this case, a strong characteristic temporal dependence of $P(\sigma^-)$ was observed as expected, while no measurable dynamics could be observed for $P(\sigma^+)$.

As the σ^- polarized signal from the lower Zeeman level exhibits no detectable dynamics over the timescales investigated, the temporal evolution of the σ^+ polarized EL intensity following σ^+ excitation (that is, $I^{\sigma^+}(t)$) was used to provide a direct measurement of the electron spin relaxation time (T_1) in QDs. Time resolved traces of $I^{\sigma^+}(t)$ in the range $\Delta t = 0.001\text{--}1\text{ ms}$ are presented in Fig. 3b for selected magnetic fields up to $B = 12\text{ T}$. For each magnetic field investigated, $I^{\sigma^+}(t)$ exhibits a mono-exponential decay,

($P < 0$) but no detectable dynamics. **b**, Semi-logarithmic plot of the temporal evolution of the co-polarized EL intensity following pumping electrons into the upper Zeeman level for different magnetic fields. T_1 and the related standard error is extracted from a least-squares mono-exponential fit of the observed decay transients.

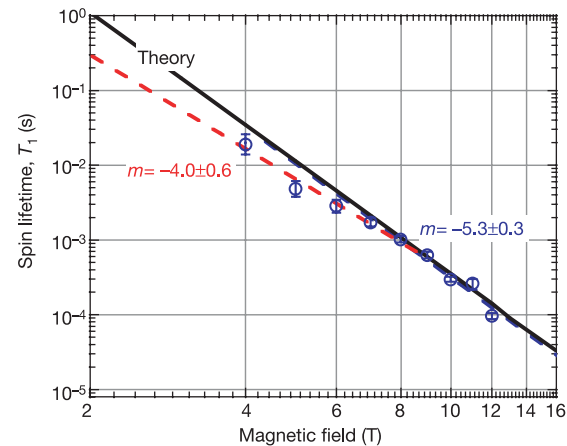


Figure 4 Double logarithmic plot of the spin lifetime T_1 versus the magnetic field at $T = 1\text{ K}$. T_1 increases from $0.1 \pm 0.01\text{ ms}$ at $B = 12\text{ T}$ to $20 \pm 6\text{ ms}$ at $B = 4\text{ T}$ (open circles). A least-squares fit of the B -field dependence for $B \geq 7\text{ T}$ (blue dashed line) reveals a power-law dependence with an exponent $m = -5.3 \pm 0.3$, suggesting that inter Zeeman level spin scattering is due to spin-orbit coupling mediated by single piezoelectric phonons as discussed in the text. Solid line: at high B -fields, the theory of refs 13 and 14 accounts remarkably well for the measured data using reasonable parameters for the investigated Ga(In)As QDs ($|g_e| = 0.8$, $\hbar\omega_0 = 30\text{ meV}$). For $B < 7\text{ T}$, a softening of the exponent to $m = -4.0 \pm 0.6$ (red dashed line) is observed owing to the increasing phonon population.

$I^{\sigma^+}(t) = I_0^{\sigma^+} \exp(-t/T_1)$, as shown by the fits in Fig. 3b. For $B < 5\text{ T}$, storage times up to $\sim 5\text{ ms}$ were measured to obtain reliable statistics. The decay time constants extracted from the data in Fig. 3b are found to be strongly dependent on the magnetic field, reducing markedly from $T_1 = 20 \pm 6\text{ ms}$ to $0.1 \pm 0.01\text{ ms}$ as the magnetic field increases from $B = 4$ to 12 T . The dependence of T_1 on the magnetic field is summarized in Fig. 4 on a double logarithmic representation. These data suggest a clear power-law dependence, $T_1 \propto B^m$, the best fit to the experimental data yielding a very large

exponent close to $m \approx -5$. We now consider the origin of this strong magnetic field dependence.

Spin-flip transitions between Zeeman levels must naturally proceed with conservation of energy, which can be ensured via the participation of acoustic phonons with an energy equal to the Zeeman energy, $E_{\text{ph}} = g_e \mu_B B$ (refs 13, 14). In this case, one-phonon scattering processes can mediate the spin-flip process by mixing of the Zeeman levels via the spin-orbit interaction^{13,14}. The spin relaxation time due to such a one-phonon admixture process in QDs has been calculated using perturbation theory^{13,14} to be:

$$\frac{1}{T_1} = A \frac{(g_e \mu_B B)^5}{\hbar(\hbar\omega_0)^4}$$

where A is a dimensionless constant that reflects the effective spin piezoelectric phonon coupling strength in the heterostructure, and $\hbar\omega_0$ is the QD single-particle level spacing. Using typical material properties applicable to GaAs (refs 13, 14) gives $A = 0.014$, which together with reasonable values for $|g_e| = 0.8$ (ref. 20) and $\hbar\omega_0 = 30$ meV (ref. 22) provide good quantitative agreement with our experimental data, as indicated by the full line in Fig. 4. The experimentally observed exponent $m = -4.9 \pm 0.2$ (not shown) is very close to the characteristic $T_1 \propto B^{-5}$ dependence expected for such one-phonon scattering processes, providing (to our knowledge) the first experimental evidence that inter Zeeman level spin-flip transitions in QDs are dominated by one-phonon scattering processes at low temperature. Closer inspection of the data presented in Fig. 4 indicates a softening of the exponent with reducing magnetic field. As shown by the blue and red dashed lines in Fig. 4, the best fit to the data for higher magnetic fields is very well described by a single exponent $m = -5.3 \pm 0.3$ (indicative of one-phonon processes, as discussed above) with the data at lower field better described by a weaker exponent $m = -4.0 \pm 0.6$. Such behaviour is expected for one-phonon processes^{13,14}, reflecting a transition between a low-temperature regime ($k_B T < g_e \mu_B B$), with the $T_1 \propto B^{-5}$ dependency discussed above, to a $T_1 \propto (k_B T)^{-1} B^{-4}$ dependency when $k_B T$ becomes comparable to $g_e \mu_B B$. In our experiment, the Zeeman splitting is comparable to the thermal energy for $B \approx 2\text{--}4$ T, in good accord with the observed softening of the exponent at low magnetic fields.

The longest T_1 time that we measured (~ 20 ms at $T = 1$ K and $B = 4$ T) is limited by the sensitivity of our detection scheme, and represents a lower limit. The absence of any observable saturation of the T_1 in Fig. 4 suggests that the relaxation time should be much longer at lower fields. For example, extrapolating the observed $T_1 \propto B^{-4}$ dependency to lower fields would indicate $T_1 = 80$ ms at ~ 3 T, reaching ~ 1 s at $B \approx 1.6$ T. However, additional spin relaxation mechanisms (such as that due to hyperfine coupling to the nuclear spin²³) will potentially limit the intrinsic T_1 times that are accessible as B approaches zero. Recent theoretical work has suggested that if spin-orbit coupling mediated by single phonons is the dominant spin scattering mechanism, then the spin coherence time should approach the limit $T_2 = 2T_1$. Our results demonstrate that this mechanism does indeed dominate, suggesting that the spin coherence times for such optically generated electrons spins may also be long.¹⁵ □

Received 9 July; accepted 10 September 2004; doi:10.1038/nature03008.

- Loss, D. & DiVincenzo, D. Quantum computation with quantum dots. *Phys. Rev. A* **57**, 120–126 (1998).
- Kane, B. E. A silicon-based nuclear spin quantum computer. *Nature* **393**, 119–120 (1998).
- Elzerman, J. M. et al. Single-shot read-out of an individual electron spin in a quantum dot. *Nature* **430**, 431–435 (2004).
- Arakawa, Y. & Tarucha, S. (eds) *Proc. 2nd Int. Conf. on Semiconductor Quantum Dots (QD 2002)*, *Physica Status Solidi B* **238** 299–372, (2003).
- Heidemeyer, H., Denker, U., Müller, C. & Schmidt, O. G. Morphology response to strain field interferences in stacks of highly ordered quantum dot arrays. *Phys. Rev. Lett.* **91**, 196103 (2003).
- Bayer, M. et al. Coupling and entangling of quantum states in quantum dot molecules. *Science* **291**, 451–453 (2001).
- Zrenner, A. et al. Coherent properties of a two-level system based on a quantum-dot photodiode. *Nature* **418**, 612–614 (2002).

- Oulton, R. et al. Manipulation of the homogeneous linewidth of an individual In(Ga)As quantum dot. *Phys. Rev. B* **66**, 045313 (2002).
- Hanson, R., Witkamp, B., Vandersypen, L. M. K., Willems van Beveren, L. H. & Elzerman, J. M. Zeeman energy and spin relaxation in a one-electron quantum dot. *Phys. Rev. Lett.* **91**, 196802 (2002).
- Fujisawa, T., Austing, D. G., Tokura, Y., Hirayama, Y. & Tarucha, S. Nonequilibrium transport through a vertical quantum dot in the absence of spin-flip energy relaxation. *Phys. Rev. Lett.* **88**, 236802 (2002); Allowed and forbidden transitions in artificial hydrogen and helium atoms. *Nature* **419**, 278 (2002).
- Meier, F. & Zakharchenya, B. (eds) *Modern Problems in Condensed Matter Sciences Vol. 8, Optical Orientation* (North Holland, Amsterdam, 1984).
- Khaetskii, A. V. & Nazarov, Y. V. Spin relaxation in semiconductor quantum dots. *Phys. Rev. B* **61**, 12639–12642 (2000).
- Khaetskii, A. V. & Nazarov, Y. V. Spin flip transitions between Zeeman sublevels in semiconductor quantum dots. *Phys. Rev. B* **64**, 125316 (2001).
- Woods, L. M., Reinecke, T. L. & Lyanda-Geller, Y. Spin relaxation in quantum dots. *Phys. Rev. B* **66**, 161318 (2002).
- Gupta, J. A., Awschalom, D. D., Peng, X. & Alivisatos, A. P. Spin coherence in semiconductor quantum dots. *Phys. Rev. B* **59**, R10421–R10424 (1999).
- Golovach, V. N., Khaetskii, A. V. & Loss, D. Phonon induced decay of the electron spin in quantum dots. *Phys. Rev. Lett.* **93**, 016601 (2004).
- Kroutvar, M. et al. Wavelength selective charge storage in self-assembled InGaAs/GaAs quantum dots. *Appl. Phys. Lett.* **83**, 443–445 (2003).
- Finley, J. J. et al. Electrical detection of optically induced charge storage in self-assembled InAs quantum dots. *Appl. Phys. Lett.* **73**, 2618–2620 (1998).
- Finley, J. J. et al. Charged and neutral exciton complexes in individual self-assembled In(Ga)As quantum dots. *Phys. Rev. B* **63**, 073307 (2001).
- Bayer, M. et al. Fine structure of neutral and charged excitons in self-assembled In(Ga)As/(Al)GaAs quantum dots. *Phys. Rev. B* **65**, 195315 (2002).
- Langbein, W. et al. Control of fine-structure splitting and biexciton binding in $In_xGa_{1-x}As$ quantum dots by annealing. *Phys. Rev. B* **69**, 161301 (2004).
- Oulton, R. et al. Continuum transitions and phonon coupling in single self-assembled Stranski-Krastanow quantum dots. *Phys. Rev. B* **68**, 235301 (2003).
- Khaetskii, A. V., Loss, D. & Glazman, L. Electron spin evolution induced by interaction with nuclei in a quantum dot. *Phys. Rev. B* **67**, 195329 (2003).

Supplementary Information accompanies the paper on www.nature.com/nature.

Acknowledgements We thank V. Golovach and D. Loss for discussions. We also thank the DFG for financial support and Attocube GmbH for technical support.

Competing interests statement The authors declare that they have no competing financial interests.

Correspondence and requests for materials should be addressed to J.J.F. (finley@wsi.tum.de).

Lead-free piezoceramics

Yasuyoshi Saito¹, **Hisaoaki Takao**¹, **Toshihiko Tani**¹,
Tatsuhiro Nonoyama², **Kazumasa Takatori**¹, **Takahiko Homma**¹,
Toshiatsu Nagaya² & **Masaya Nakamura**²

¹Toyota Central R&D Laboratories, Inc., Nagakute, Aichi, 480-1192, Japan

²DENSO Corporation, 1-1, Showa-cho, Kariya, Aichi, 448-8861, Japan

Lead has recently been expelled from many commercial applications and materials (for example, from solder, glass and pottery glaze) owing to concerns regarding its toxicity. Lead zirconium titanate (PZT) ceramics are high-performance piezoelectric materials, which are widely used in sensors, actuators and other electronic devices; they contain more than 60 weight per cent lead. Although there has been a concerted effort to develop lead-free piezoelectric ceramics, no effective alternative to PZT has yet been found^{1–14}. Here we report a lead-free piezoelectric ceramic with an electric-field-induced strain comparable to typical actuator-grade PZT. We achieved this through the combination of the discovery of a morphotropic phase boundary in an alkaline niobate-based perovskite solid solution, and the development of a processing route leading to highly $\langle 001 \rangle$ textured polycrystals. The ceramic exhibits a piezoelectric constant d_{33} (the induced charge per unit force applied in the same

Copyright of Nature is the property of Nature Publishing Group and its content may not be copied or emailed to multiple sites or posted to a listserv without the copyright holder's express written permission. However, users may print, download, or email articles for individual use.